UC San Diego
UC San Diego Previously Published Works

Title

Liquefied gas electrolytes for wide-temperature lithium metal batteries

Permalink

Journal

Energy & Environmental Science, 13(7)

ISSN

Authors

Yang, Yangyuchen
Yin, Yijie
Davies, Daniel M
et al.

Publication Date

2020-07-15

DOI

Peer reviewed

PAPER

Check for updates

Liquefied gas electrolytes for wide-temperature lithium metal batteries†

Yangyuchen Yang,[a] Yijie Yin,[a] Daniel M. Davies,[b] Minghao Zhang,[b] Matthew Mayer,[b] Yihui Zhang,[a] Ekaterina S. Sablina,[a] Shen Wang,[b] Jungwoo Z. Lee,[c] Oleg Borodin, ID *[de] Cyrus S. Rustomji*[c] and Y. Shirley Meng ID *[ab]

The momentum in developing next-generation high energy batteries calls for an electrolyte that is compatible with both lithium (Li) metal anodes and high-voltage cathodes, and is also capable of providing high power in a wide temperature range. Here, we present a fluoromethane-based liquefied gas electrolyte with acetonitrile cosolvent and a higher, yet practical, salt concentration. The unique solvation structure observed in molecular dynamics simulations and confirmed experimentally shows not only an improved ionic conductivity of 9.0 mS cm^{-1} at +20 °C but a high Li transference number (t_{Li^+} = 0.72). Excellent conductivity (>4 mS cm^{-1}) was observed from −78 to +75 °C, demonstrating operation above fluoromethane's critical point for the first time. The liquefied gas electrolyte also enables excellent Li metal stability with a high average coulombic efficiency of 99.4% over 200 cycles at the aggressive condition of 3 mA cm^{-2} and 3 mA h cm^{-2}. Also, dense Li deposition with an ideal Li–substrate contact is seen in the liquefied gas electrolyte, even at −60 °C. Attributed to superior electrolyte properties and the stable interfaces on both cathode and anode, the performances of both Li metal anode and Li/NMC full cell (up to 4.5 V) are well maintained in a wide-temperature range from −60 to +55 °C. This study provides a pathway for wide-temperature electrolyte design to enable high energy density Li–metal battery operation between −60 to +55 °C.

1. Introduction

Increasing adoption of EV, UAVs and portable electronics leads to increasing demand for lithium-ion batteries operating over a wide temperature range.[1,2] To further boost energy density and reduce cost, researchers revisited lithium metal batteries (LMBs) because of the highest achievable gravimetric energy density of lithium metal.[3,4] However, among the several challenges limiting the applications of LMBs is the development of an electrolyte that is stable with both the Li-metal anode and high-voltage cathodes in a wide temperature range (−60 to +55 °C).[5,6]

[a] *Materials Science and Engineering, University of California San Diego, La Jolla, CA 92121, USA. E-mail: shmeng@ucsd.edu*
[b] *Department of Nano Engineering, University of California San Diego, La Jolla, CA 92121, USA*
[c] *South 8 Technologies, Inc., San Diego, CA 92109, USA. E-mail: crustomji@south8technologies.com*
[d] *Electrochemistry Branch, Sensors and Electron Devices Directorate, U.S. Army Research Laboratory, Adelphi, MD 20783, USA. E-mail: oleg.a.borodin.civ@mail.mil*
[e] *Joint Center for Energy Storage Research, U.S. Army Research Laboratory, Adelphi, MD 20783, USA*
† Electronic supplementary information (ESI) available. See DOI: 10.1039/d0ee01446j

Extensive efforts have been devoted to improving the electrolyte formulations to make them compatible with more aggressive higher energy density anode–cathode couples.[7–10] Commercialized ethylene carbonate (EC)-based electrolytes have moderate oxidation stability (∼4.3 *versus* Li) for cathode operation. However, EC-based electrolytes have issues of dendrite formation and low coulombic efficiency (CE) with Li-metal anode, along with a narrow operational temperature range, only down to −20 °C due to high melting point of EC of 35 °C.[7] Ether-based electrolytes show improved compatibility with the Li-metal anode and low-temperature performance due to the formation of a relatively favorable SEI and the lower melting point. Yet, the low oxidation stability (<4.0 *versus* Li) prevents its potential applications.[11] In recent years, high-concentration electrolytes have been shown to be able to stabilize Li-metal anode and cathodes by reducing the amount of free solvent and manipulating the interphase composition.[12–14] However, these high concentration electrolytes sacrifice cost, viscosity, wetting, and low-temperature operation. Localized high-concentration electrolytes (LHCE) were developed by diluting electrolytes with different non-solvating solvents, which presented more balanced properties.[15,16] For example, the use of fluorinated non-polar diluents (1,1,2,2-tetrafluoroethyl-2′,2′,2′-trifluoroethyl ether, HFE) in concentrated fluorinated electrolytes with an

This journal is © The Royal Society of Chemistry 2020

Energy Environ. Sci., 2020, **13**, 2209–2219 | **2209**

optimized ratio demonstrated stable interfaces with Li–metal batteries and impressive low-temperature performance down to −85 °C.[17,18] Nevertheless, the low-temperature conductivity was quite low (0.011 mS cm^{-1} at −80 °C) and the reported cells were charged at room temperature and only discharged at low temperatures. Also, the Li-metal anode's low-temperature performances, such as deposition morphology, CE, have not been verified separately.[18] At the same time, nitrile-based electrolytes regained attention: acetonitrile's (AN) stability with Li-metal anode has been improved by increasing the salt concentration, limiting the free AN molecules.[19,20] AN and other nitrile-based solvents were also used as cosolvents to improve the stability and the low-temperature performance of both aqueous electrolyte and non-aqueous electrolytes.[21] Additionally, recent studies[22–24] have shown that the solvation of Li ion has significant impact on the properties of the electrolyte and interface formation. Understanding and formulating the solvation structure of electrolyte are the key for developing next-generation electrolyte.

The recently developed fluoromethane (CH$_3$F, FM)-based liquefied gas electrolytes demonstrated an impressive low-temperature operation down to −60 °C and good stability with both a Li-metal anode and a 4 V class cathode.[25] This can be attributed to its unique physical and chemical properties, including low melting point, low viscosity and ability to form F-rich SEI/CEI. The electrolyte performance was further enhanced by the introduction of tetrahydrofuran (THF) as a cosolvent to improve the salt solubility and the conductivity.[26] The unique solvation structure presented an impressive Li-metal efficiency at both room temperature (99.6%) and low temperature (98.5% at −60 °C) using a current density of 0.5 mA cm^{-2} and 1 mA h cm^{-2}. Interestingly, a sudden drop in conductivity was observed when the temperature reached FM's critical point ($T_{c,FM}$ = +44 °C). This phenomenon has been identified as a potential reversible battery shut-down mechanism, yet this shutdown temperature is relatively low for many

applications. Additionally, although the THF cosolvent is fully coordinated with Li salt, it still limits the further improvement of the oxidation stability.

Herein, we formulated liquefied gas electrolytes using AN as a cosolvent and enabled a higher, yet practical salt concentration of 1.2 M bis(trifluoromethane)sulfonimide (LiTFSI) for high-voltage Li–metal batteries in a wide temperature range. The electrolyte shows impressive ionic conductivity in wide temperatures ranging from −78 to +75 °C. The new solvation structure expanded the liquefied gas electrolyte's high-temperature range beyond FM's critical point for the first time. This work also demonstrates the use of liquefied gas electrolyte for stable cycling of both Li-metal anode and 4.5 V Li–metal batteries in temperatures extending from −60 to +55 °C.

2. Results and discussion

2.1. Ion transport and solvation of the electrolytes

AN was selected as a cosolvent for FM solvent due to its high dielectric constant, low viscosity, and good oxidation stability.[19] Solubility tests were first performed with a salt-to-cosolvent molar ratio close to 1 : 1 to ensure LiTFSI is fully dissolved. The high-pressure window cell clearly shows there is no phase separation of the LiTFSI–AN–FM mixture up to 1.2 M LiTFSI, 1 M AN in FM (Fig. 1A). With this high salt-to-cosolvent ratio (1.2 : 1), AN is thought to be fully coordinated with Li cations (Fig. 1B) and is expected to improve its stability with Li metal anode at the same time.[19] FM is also expected to partially coordinated with Li cations due to its relatively lower affinity. Therefore, the solvation structure model is proposed in Fig. 1B and is further investigated in later characterization sections.

Ionic conductivity measurements of the liquefied gas electrolytes at different salt concentrations were performed (Fig. 1C). Similar to previous observations,[25,26] the conductivity at low salt and cosolvent concentration is well maintained at low
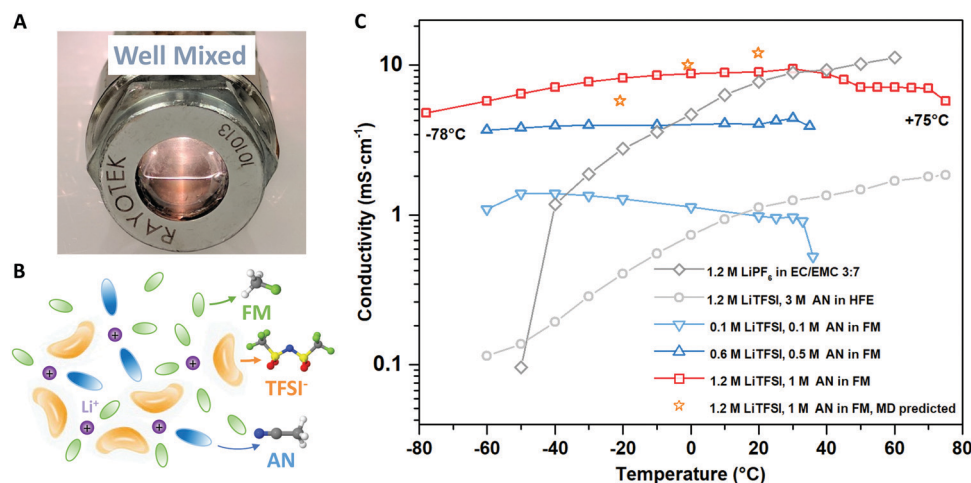

Fig. 1 Design and conductivity of liquefied gas electrolyte (A) solubility test in a window cell of 1.2 M LiTFSI, 1 M AN in FM. (B) Schematic illustration of the solvation structure of liquefied gas electrolyte. (C) Ionic conductivity of liquefied gas electrolytes with different salt and cosolvent concentrations from experiments and the MD simulations predictions for 1.2 M LiTFSI, 1 M AN in FM.

temperatures down to −60 °C. But as demonstrated by observations from the window cells (Fig. S1 and S2, ESI†), when temperature closes to FM's critical point ($T_{c,FM}$ = +44 °C), the most of FM goes to supercritical state and little liquid is left. Although the liquid left is still a mixture of LiTFSI–AN–FM and should have conductivity, it's impracticable for conductivity measurement and cell cycling. Notably, at higher salt and cosolvent concentrations of 1.2 M LiTFSI and 1 M AN, a substantially different conductivity curve is observed. The electrolytic conductivity of 1.2 M LiTFSI, 1 M AN in FM shows a conductivity of 9.0 mS cm^{-1} at +20 °C, which is comparable to most conventional liquid electrolytes. FM and AN's low viscosity (η_{FM} = 0.085 mPa s, η_{AN} = 0.37 mPa s) and low melting point ($T_{m,FM}$ = −142 °C, $T_{m,AN}$ = −44 °C), coupled with the higher salt concentration enables an impressive low-temperature electrolytic conductivity of 5.8 mS cm^{-1} at −60 °C and 4.8 mS cm^{-1} at −78 °C. These low-temperature conductivity values compare favorably with most known electrolytes, including previously reported liquefied gas electrolyte (3.9 mS cm^{-1}, −60 °C),[26] ethyl acetate-based electrolytes (0.2 and 0.6 mS cm^{-1}, −70 °C),[27,28] and fluorinated localized high concentration electrolyte based on the carbonate solvent

(0.044 mS cm^{-1}, −70 °C)[18] and AN solvent (Fig. 1C and Fig. S2, ESI†). Furthermore, the conductivity is still well-maintained at high-temperatures up to +75 °C (5.7 mS cm^{-1}), which is sufficient for most high-temperature applications. The wider temperature range is thought to be related to increasing the amount of salt and cosolvent, which may reduce volume change and maintain increasing amount of FM in LiTFSI–AN–FM mixture (Fig. S3, ESI†), allowing operation above FM's critical point. The internal pressure above the critical point is also expected to be reduced by the extra amount of cosolvent and salt. Additionally, in a separate study, strategies to further decrease the operating pressure have been demonstrated and will be published in future work.

The solvation structure of the liquefied gas electrolyte was investigated *via* Raman spectroscopy and molecular dynamics (MD) simulations. To identify the coordination of Li$^+$ with AN and FM molecules, Raman spectra were obtained for the 1 M AN co-solvent in FM at various LiTFSI concentrations (0 M to 1.2 M) (Fig. 2A–C and Fig. S4, ESI†). As shown in Fig. 2A, the peak of C≡N is located at 2252 cm^{-1}, derived from the pure AN solvent. By increasing the amount of salt, the normalized intensity of the peak at 2252 cm^{-1} gradually decreases, whereas
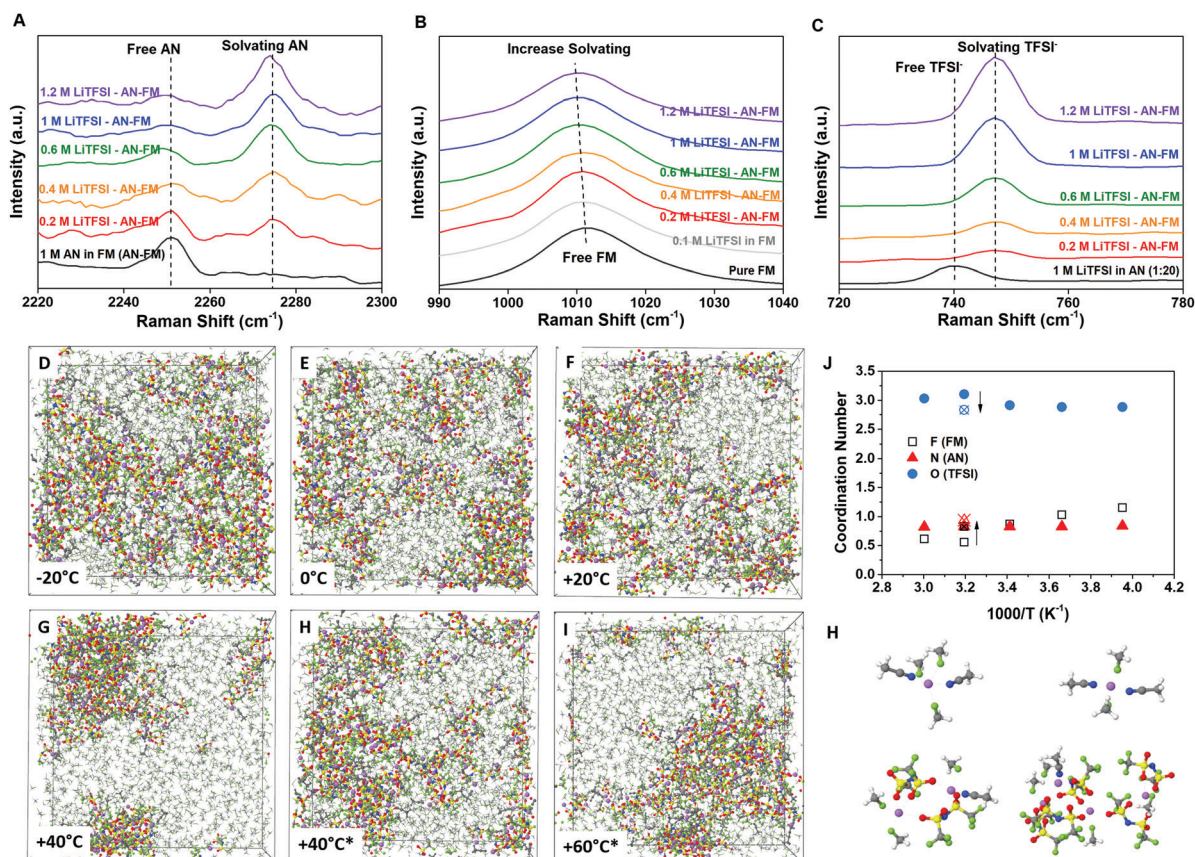

Fig. 2 Solvation structure of bulk electrolyte (A–C) Raman spectra of liquefied gas electrolytes with 1 M AN and increasing LiTFSI concentrations in 2220–2300 cm^{-1} (C–N stretching vibration of AN molecules), 990–1040 cm^{-1} (C–F stretching vibration of FM molecules), and 720–780 cm^{-1} (S–N–S bending vibration of TFSI$^-$). (D–I) Snapshots of the MD simulations cells of 1.2 M LiTFSI–AN–FM electrolyte using experimental densities (D–G) and compressed electrolytes (H and I) denoted with (*), color: Li$^+$, purple; O, red; C, gray; H, white; N, blue; S, yellow; F, green. (J) Coordination numbers *versus* temperatures of FM, AN, and TFSI$^-$ molecules (crossed symbols denote the compressed system). (K) Representative solvates for the free Li$^+$ and ionic aggregates.

This journal is © The Royal Society of Chemistry 2020

Energy Environ. Sci., 2020, **13**, 2209–2219 | **2211**

a different peak at 2270 cm^{-1} appears (Fig. 2A). The appearance of this additional peak is attributed to the formation of AN–Li$^+$ solvation structure.[29] At salt concentrations above 1 M, AN's strong coordination with the Li$^+$ and near absence of free AN is believed to improve oxidation stability of AN and stabilize its interface with Li metal.[19] The interaction of Li$^+$ and FM was also detected in Fig. 2B. Although solubility of LiTFSI in FM is low ($<$0.1 M), a red-shift of the C–F stretching peak (around 1012 cm^{-1}) is observed after adding 0.1 M LiTFSI into pure FM, indicating the bond order of C–F had been impaired as the fluorine's lone electron pair coordinate to lithium ion. Furthermore, with 1 M AN and increasing amount of LiTFSI, the C–F peak moves to a lower frequency (around 1010 cm^{-1}). It is likely because more LiTFSI is dissolved with the present of AN, therefore enabling more FM–Li$^+$ coordination. Unlike the inert dilutes seen in the localized high concentration electrolytes that not participate the solvation shell and have slow transport kinetics due to their relatively large size,[15,30] the slightly solvating feature of FM–Li$^+$ in liquefied gas electrolytes together the small size of FM provides extra benefits for the rapid ion transport and desolvation, especially at low temperatures. Raman spectrum of TFSI$^-$ in the 740–755 cm^{-1} region is particularly sensitive to the Li$^+$ coordination, with a band near 740 cm^{-1} assigned to free TFSI$^-$ and 746–753 cm^{-1} is assigned to aggregates.[31] Following this assignment, Fig. 2C indicates that most TFSI$^-$ anions in dilute LiTFSI–AN (1:20) exist as free anions, while in the LiTFSI–AN–FM electrolytes the TFSI$^-$ anions participate in aggregates due to the high salt-to-cosolvent ratio.[29] The low free TFSI$^-$ indicates a high Li$^+$ transference number measuring experimentally using Bruce–Vincent method[32] (t_{Li^+} = 0.72, Fig. S5, ESI†). Solvated TFSI$^-$ is believed to have higher reduction activity over free TFSI$^-$, leading to a favorable interphase for stable Li-metal cycling.[33,34]

MD simulations were performed on the 1.2 M LiTFSI, 1 M AN in FM electrolyte in order to obtain further insight into the solvation structure and Li$^+$ transport. Representative snapshots (Fig. 2D–I) show that at low temperature (-20 °C) ions are distributed rather uniformly throughout the simulation cell but start slowly separating into the ion-rich domain with increasing ion aggregation and ion-poor domains as temperature increases. Such increased ion aggregation results in the eventual conductivity drop at high temperatures. Note that two different snapshots are shown for +40 °C corresponding to two different densities: one approximated from experiments at +40 °C, while the other corresponds to the compressed electrolyte having a density estimated from measurements at +20 °C but simulated at +40 °C (Computational methods). Electrolyte compression (compare Fig. 2G *vs.* Fig. 2H) leads to homogenization of the ion domains, changes in the Li solvation shell and ion transport, which agrees well with previously reported phenomena under liquefied gas electrolytes.[25,35] Analysis of the radial distribution functions (RDFs) (Fig. S6, ESI†) indicates a strong preference for the Li$^+$ to be coordinated by AN followed by the oxygen atoms of TFSI with a smallest peak observed for the Li–F(FM). Based on RDFs we chose 2.8 Å as a first solvation shell of the Li$^+$ cations (Fig. 2J) that comprised, on average,

of 2.9 O(TFSI) and 0.83 of AN and 0.89 of FM. The Li$^+$ coordinates to $\sim$3 oxygen atoms of TFSI coming from two TFSI$^-$ anions, one of which has monodentate binding to a Li$^+$ (Fig. 2K) while the other has a bi-dentate binding to Li$^+$ giving rise to an extended chain of aggregates, especially at higher temperatures $>$+20 °C (Fig. S7, ESI†). Notably, electrolyte compression results in dissociation of the larger aggregates and increases free ion population. Absence in MD simulations of free TFSI$^-$ and free AN, that is not coordinated to a Li$^+$, is in excellent agreement with Raman spectra (Fig. 2A and C),

Fig. 2J shows that the number of AN around Li$^+$ is temperature independent and is equal to the ratio of AN to LiTFSI (0.83) further confirming that nearly all available AN solvents are participating in the Li$^+$ solvation in excellent agreement with interpretation Raman spectra shown in Fig. 2A. Interestingly, not all Li$^+$ have the same number of AN around it. Free Li$^+$ cation (not coordinated to TFSI) tend to have 2 AN and 2–3 FM solvents (Fig. S8, ESI†), thus AN disproportionately contributes to coordination of free Li$^+$ at the expense of coordinating Li$^+$ in ionic aggregates, which is consistent with the representative free Li$^+$ and aggregate solvates shown in Fig. 2K. As a result of this preference of AN to free Li$^+$, even in a highly deficient AN co-solvent regime (AN : Li $<$ 1.0) a substantial fraction of free Li$^+$ exists (Fig. S9, ESI†) leading to high Li$^+$ conductivity.

A temperature dependence of the fraction of free lithium cations correlates well with the degree ion ionic correlated motion (ionicity) (Fig. S9, ESI†), clearly indicating a drop of free ions at higher temperature. Further compression at the highest temperatures, not only increases ionic dissociation but also prevents a drop in ion diffusion coefficients due to ion aggregation (Fig. S10, ESI†) resulting in a conductivity improvement (Table S1, ESI†). Due to low viscosity of the main solvent (FM) and much higher diffusion of free Li$^+$ compared to ionic aggregates, vehicular motion of the Li$^+$(AN)$_2$(FM)$_n$, n = 2 or 3 is the dominant diffusion mechanism. Also, the residence time for Li–FM (32 ps) is much shorter than Li–AN (7407 ps) and Li–N(TFSI) (6926 ps) (Fig. S11, ESI†), indicating the rapid ion transport from FM and supporting the vehicular mechanism for the free Li$^+$ motion. Indeed, Fig. S12 (ESI†) shows that diffusion of free Li$^+$ is 4 times higher than average Li$^+$ ion diffusion. Finally, because there is essentially no free TFSI$^-$ anions ($<$0.3% at all temperatures, unlike Li$^+$) most charge transport occurs *via* Li$^+$(AN)$_2$(FM)$_n$ diffusion leading to high Li$^+$ transference number estimated from MD simulations ($>$0.94).

2.2. Li metal anode performance

To explore the compatibility of the proposed electrolyte with Li metal anode, Li metal plating and stripping tests were performed. 1 M lithium bis(fluorosulfonyl)imide (LiFSI) in 1,2 dimethoxyethane (DME) was selected as the ether baseline electrolyte due to its well-known compatibility with the Li metal anode. 1.2 M LiPF$_6$ in ethylene carbonate/ethylmethyl carbonate (1.2 M LiPF$_6$ EC/EMC 3:7) was selected as a carbonate baseline electrolyte, as its higher linear carbonate ratio enables an improved low-temperature performance compared to other conventional liquid electrolytes.[7] An aggressive rate of 3 mA cm^{-2}

2212 | *Energy Environ. Sci.*, 2020, **13**, 2209–2219

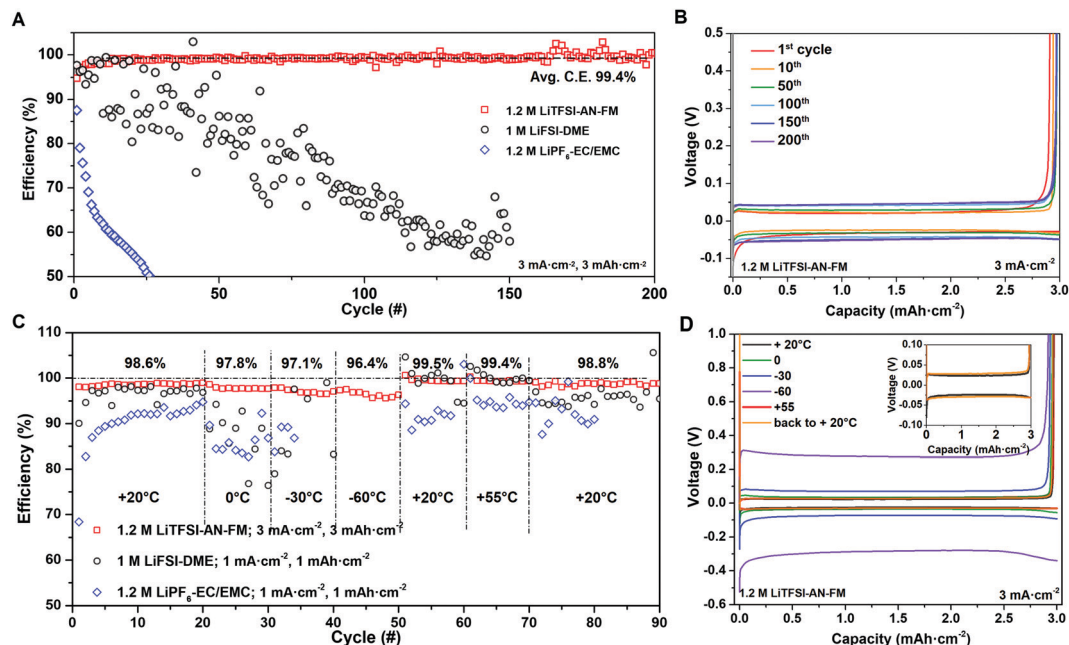This journal is © The Royal Society of Chemistry 2020

Fig. 3 Electrochemical performance of Li metal anode in liquefied gas electrolyte at different temperatures (A) the CE of Li metal plating/stripping over 200 cycles in various electrolytes, (B) voltage profiles for the cell using liquefied gas electrolyte used in (A). (C) The CE of Li metal plating and stripping at various temperatures, (D) voltage profiles for the cell using liquefied gas electrolyte used in (C).

with a practical capacity of 3 mA h cm^{-2} was selected in order to push the limit of this liquefied gas electrolyte.[36] As shown in Fig. 3A, at 3 mA cm^{-2} and 3 mA h cm^{-2}, the CE in the liquefied gas electrolyte (1.2 M LiTFSI, 1 M AN in FM : CO$_2$ 19 : 1, labeled as 1.2 M LiTFSI–AN–FM) increased to >99.1% within the first 20 activation cycles and stable Li plating–stripping was demonstrated up to 200 cycles with an average CE of 99.4%. The minimal increase in overpotential (Fig. 3B) indicates the SEI formed from liquefied gas electrolyte remains stable even with such a high current density and capacity cycling. In contrast, 1 M LiFSI–DME, 1.2 M LiPF$_6$–EC/EMC (Fig. 3A), and 1.2 M LiTFSI, 3 M AN in HFE (Fig. S13, ESI†) showed inferior CEs and quick fading, suggesting their poor stability and kinetic limitations.

To further evaluate the Li metal anode performance in a wide temperature range, extended cycling of the Li-metal anode was performed from −60 to +55 °C (Fig. 3C). Using the same aggressive cycling conditions (3 mA cm^{-2} and 3 mA h cm^{-2}), the stable Li metal plating/stripping in the liquefied gas electrolyte was maintained in a wide temperature range, showing an average CE of 96.4% at −60 °C and 99.4% at +55 °C with an overpotential of 310 mV and 28 mV, respectively. After being brought back to room temperature, due to the little effect on the electrolyte and interface properties when exposed to the low and high temperatures, the voltage curve of the Li metal anode matched well with its initial state (Fig. 3D). As a comparison, ether-based electrolyte and carbonate-based electrolyte show the inferior performance in a narrower temperature range, even under lower current density and capacity (1 mA cm^{-2} and 1 mA h cm^{-2}). The latter electrolytes showed an unstable plating and stripping curve at 0 and −30 °C (Fig. S14, ESI†), resulting in large fluctuations of CE. Additionally, both cells

were unable to cycle at lower temperatures and showed reduced performance after high-temperature cycling.

2.3. Li metal structures

The surface morphology and the cross-sectional structure of Li metal deposited in various electrolytes were observed via scanning electron microscopic (SEM) and cryogenic focused ion beam (cryo-FIB). To overcome the difficulties of Li metal characterization due to its high reactivity and low atomic number, cryo-FIB was implemented to minimize the damage and avoid morphological artifacts.[26,37] The samples were prepared with a capacity of 3 mA h cm^{-2} at 0.5 mA cm^{-2}, which is close to many potential application scenarios and corresponds to a deposition thickness of ∼15 μm for ideal dense Li metal.

The electrochemically deposited lithium surface and the bulk morphologies were greatly affected by electrolyte formulations (Fig. 4A–H). Consistent with literature, the carbonate-based electrolyte formed needle-like dendrites (Fig. 4A) with a non-uniform distribution, which leads to a porous bulk structure with high tortuosity and bad structural connections (Fig. 4E). As shown in Fig. 4B, dendrite-free deposited Li with large roundly shaped Li particles was enabled by the ether-based electrolyte. Despite the favorable top-view morphology, the cross-section exhibited a large number of voids in the bulk structure, resulting in a relatively high structural tortuosity (Fig. 4F). However, the Li deposited in the liquefied gas electrolyte demonstrated a roundly shaped, densely packed dendrite free surface (Fig. 4C). Although the primary particle size is slightly smaller than the one generated by the ether-based electrolyte, the bulk structure is largely improved. The liquefied
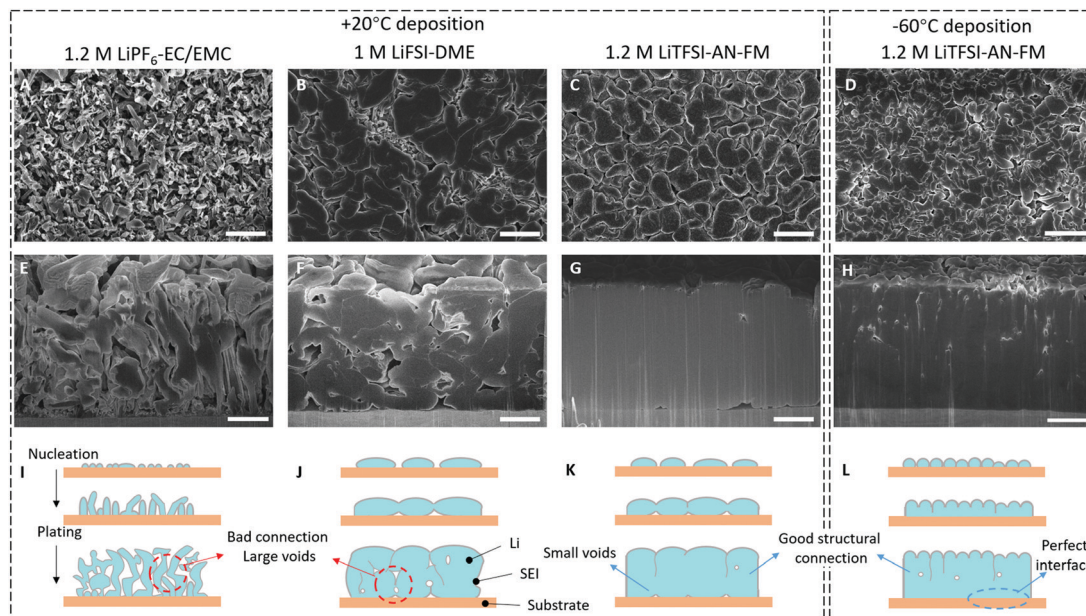
This journal is © The Royal Society of Chemistry 2020

Energy Environ. Sci., 2020, **13**, 2209–2219 | **2213**

Fig. 4 Cryo-FIB characterization of the morphologies of electrochemically deposited Li (A–D) top-view SEM images (A–C, scale bar 10 μm; (D) scale bar 5 μm), (E–H) cross-sectional SEM images (scale bar 4 μm) of deposited Li, and its schematic illustration (I–L). The Li metal was plated in 1.2 M LiPF$_6$–EC/EMC (A, E and I), 1 M LiFSI–DME (B, F and J), and 1.2 M LiTFSI–AN–FM (C, G and K), at a current density of 0.5 mA cm^{-2} with a capacity of 3 mA h cm^{-2} at room temperature. Li metal in (D, H and L) is deposited at −60 °C in the same liquified gas electrolyte, current and capacity.

gas electrolyte presents a very dense Li deposition, aside for a few small voids on the Li/substrate interface formed during nucleation (Fig. 4G). This indicates that the Li growth during deposition is completely uniform, which may be attributed to the high kinetics of the electrolyte and the stable interface. Further, the differences in surface morphology between the conventional liquid electrolyte and the liquefied gas electrolyte become even more apparent after several cycles (Fig. S15, ESI†).

The morphology of Li deposited at low temperature (−60 °C) was also investigated in 1.2 M LiTFSI–AN–FM (Fig. 4D and H). The primary particle deposited at low temperature has a smaller size, which is consistent with previous studies.[38,39] Literature has shown that dendrites are easier to form at low temperatures (< −20 °C) in most of the electrolytes due to the smaller nucleation size and sluggish Li$^+$ diffusion.[38,39] However, even at −60 °C, the liquified gas electrolyte supports roundly shaped primary particles and a dense Li deposition with a close contacted Li–substrate interface, in which barely any voids are observed (Fig. 4H and Fig. S16, ESI†). It is believed that the smaller nucleation size at lower temperature enhances the Li–substrate contact by eliminating the voids seen at room temperature while the dense dendrite-free deposition is maintained due to the fast kinetics of liquefied gas electrolyte at low temperatures. The described Li deposition models are illustrated in Fig. 4I–L. The structure by liquefied gas electrolyte agrees well with the recent proposed ideal Li metal structure.[40] The chunky morphology and low tortuosity of deposited Li in the liquefied gas electrolyte enables an ideal structural connection, and therefore, explains the high CE and stability even at high current and low-temperature.

2.4. Electrochemical performance of Li metal batteries

Li–LiNi$_{0.6}$Mn$_{0.2}$Co$_{0.2}$O$_2$ (NMC622) full cells with an areal loading of ~1.8 mA h cm^{-2} were then used to investigate the anodic stability of the various electrolytes. The improved liquefied gas electrolyte showed high anodic stability up to 4.5 V in Li–NMC voltage hold test (Fig. S17, ESI†). At a cutoff voltage of 4.3 V, the Li–NMC cell had a discharge capacity of 167 mA h g^{-1} and enables > 96.5% capacity retention after 500 cycles with an average CE of 99.7% (Fig. 5A and B). In contrast, carbonate-based and ether-based electrolyte displayed quick fading and limited capacity retention after 200 cycles. When the cutoff voltage was increased to 4.5 V, an initial discharged capacity of 191 mA h g^{-1} with a > 91.5% capacity retention was still maintained after 200 cycles, resulting an average CE of 99.5% (Fig. S18, ESI†). In the liquefied gas electrolyte, the Al corrosion by imide salt (LiTFSI/LiFSI) was also largely reduced (Fig. S19, ESI†) because of the absence of free AN in electrolyte as all AN solvent molecules are bound to Li$^+$. The only free solvent is a fluorinated FM solvent with a low solvation power for the Al corrosion products and containing fluorine to passivate the Al surface.[41,42]

Cyclic voltammetry (CV) tests of Li–NMC full cells were then performed on different electrolytes to investigate the kinetic behavior at lower temperatures (Fig. 5C and F). At +20 °C, 1.2 M LiTFSI–AN–FM and 1.2 M LiPF$_6$–EC/EMC electrolyte showed similar de-lithiation and lithiation peaks. However, at lower temperatures, 1.2 M LiPF$_6$–EC/EMC electrolyte experienced a large voltage shift at −30 °C and no redox peak was observed at −60 °C, suggesting a higher resistance and slower kinetics occur at lower temperature. In contrast, the use of liquefied gas electrolyte showed a smaller peak shift in comparison to the
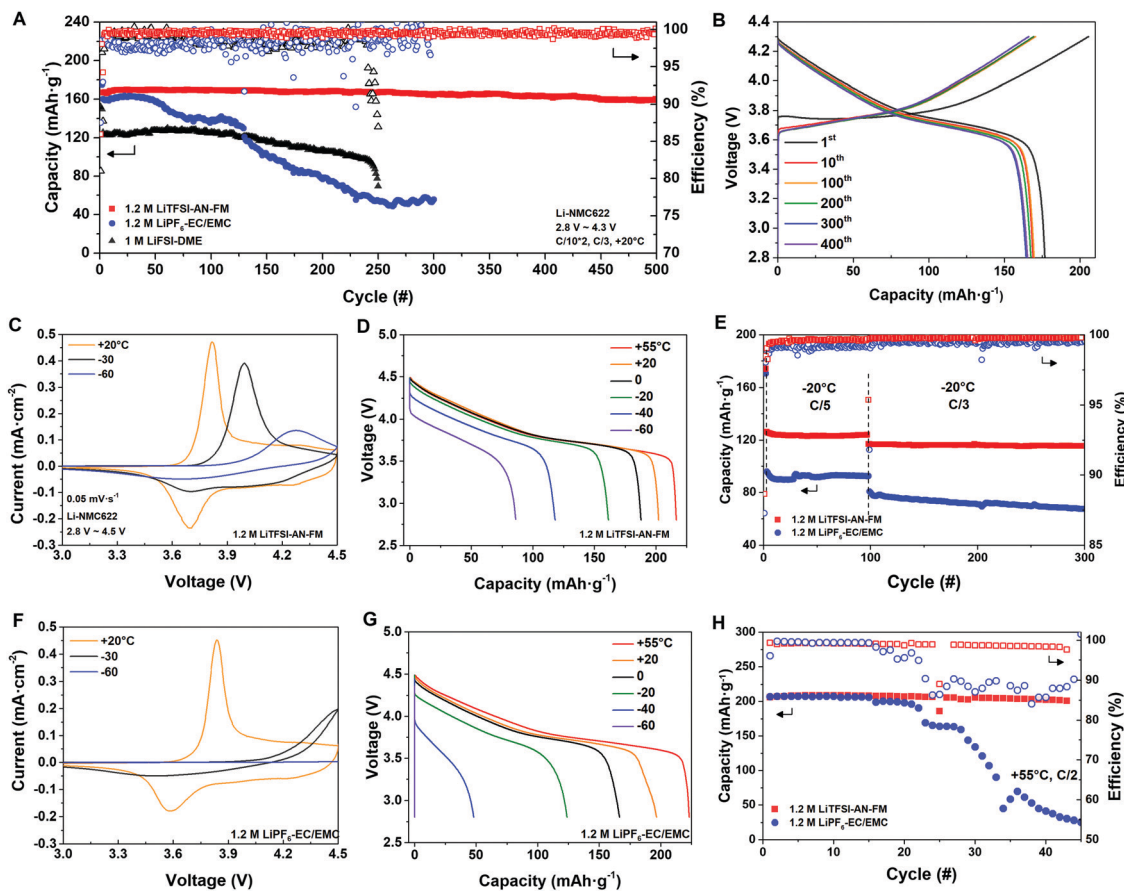
Fig. 5 Electrochemical performance of Li–NMC622 cells in wide temperature range (A) cycling performance of Li–NMC622 in different electrolytes, (B) the charge–discharge curves of the cell using liquefied gas electrolyte in (A). Cyclic voltammetry curves (C) and discharge profiles (D) of Li–NMC at different temperatures using 1.2 M LiTFSI–AN–FM. (E) Cycling performance of Li–NMC622 at −20 °C with different electrolytes. (F and G) Cyclic voltammetry curves (F) and discharge profiles (G) of Li–NMC at different temperatures using 1.2 M LiPF$_6$–EC/EMC. (H) Charge–discharge curves of Li–NMC cycling at +55 °C.

carbonate electrolyte and the charging/discharging processes are clearly observed even at −60 °C. This behavior is indicative of the rapid kinetics through bulk electrolyte and interfaces, illustrating improved low-temperature performance. To simulate real battery applications, all cells in cycling tests were charged and discharged at the same temperature, rather than charged at room temperature followed by low-temperature discharge.[18,27] The discharge behavior of the Li–NMC622 cells with the carbonate and 1.2 M LiTFSI–AN–FM electrolytes was systematically studied over a wide temperature range as shown Fig. 5D and G. Although the 1.2 M LiPF$_6$–EC/EMC electrolyte showed a similar capacity of ∼200 mA h g^{-1} at +20 °C and rate of C/15, the Li–NMC cell in the carbonate electrolyte could deliver only <25% capacity retention at −40 °C and could not deliver any capacity at −60 °C. However, the use of 1.2 M LiTFSI–AN–FM liquefied gas electrolyte enabled 60% and 45% capacity retention at −40 °C and −60 °C, respectively. Note that if the cell was charged at room temperature, a higher capacity of 65% can be achieved at −60 °C (Fig. S20, ESI†). This difference highlights the significance of temperature on the charging process. The capacity improvement from room temperature charging is likely due to the kinetic barrier during low

temperature charging. This kinetic barrier may lead to issues in some electrolytes, even if they show reasonable low-temperature discharge performance. In low temperature (−20 °C) long-term cycling, the Li–NMC cells using 1.2 M LiTFSI–AN–FM shows excellent stability and the capacity is 36% and 52% higher than the cells using 1.2 M LiPF$_6$–EC/EMC at C/5 and C/3 rate, respectively (Fig. 5E). This superior low-temperature performance is also highlighted by a Li–NMC full cell using liquefied gas electrolyte powering a LED light at temperatures as low as −78 °C in dry ice (Fig. S21, ESI†).

The liquefied gas electrolyte with increased amount of salt and cosolvent also demonstrated improved high-temperature operation. When the temperature was increased to +55 °C, the cell using the liquefied gas electrolyte showed a similar discharge curve (Fig. 5D and G) and redox process (Fig. S22, ESI†), with slightly faster kinetics than the cell using the 1.2 M LiPF$_6$–EC/EMC. In subsequent charge/discharge cycles, the Li–NMC cell in 1.2 M LiTFSI–AN–FM maintained high capacity retention at around 200 mA h g^{-1}, while the liquid cell using 1.2 M LiPF$_6$–EC/EMC started to decay in less than 20 cycles (Fig. 5H and Fig. S23, ESI†). This fading may result from the
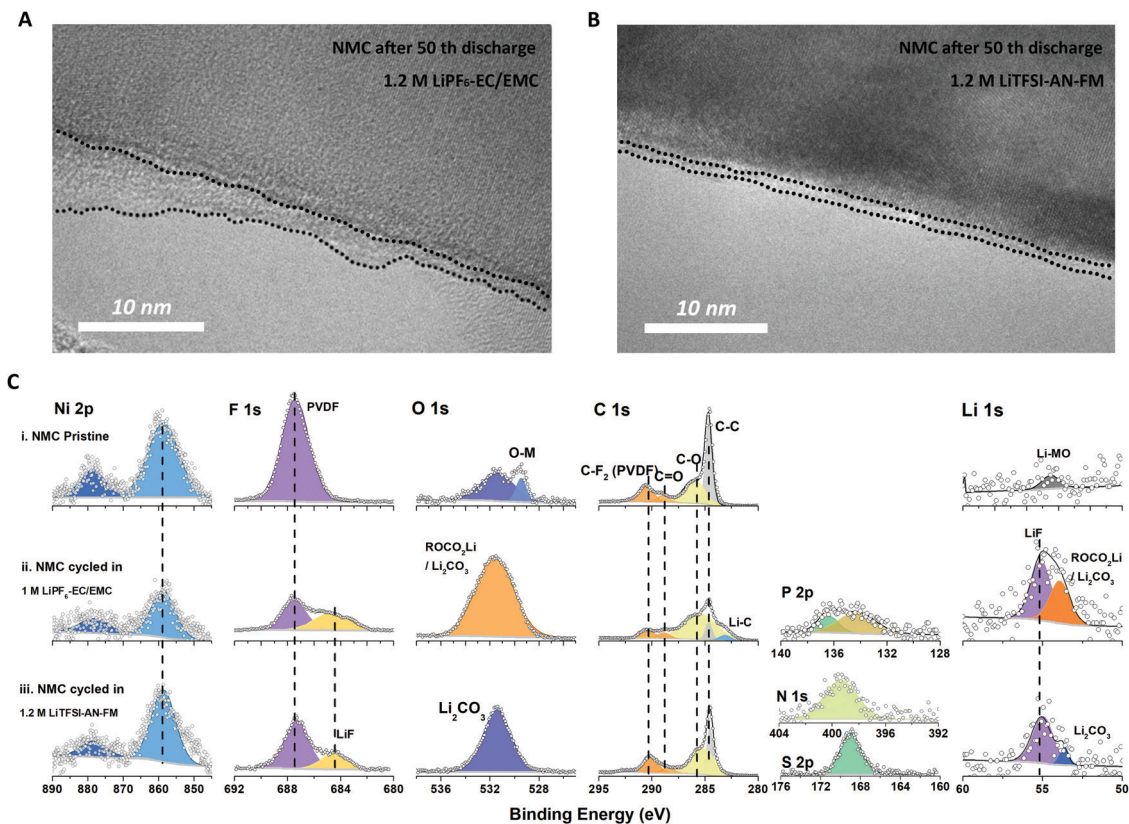
This journal is © The Royal Society of Chemistry 2020

Energy Environ. Sci., 2020, **13**, 2209–2219 | **2215**

Fig. 6 Interfaces characterizations of cycled NMC622 (A and B) cryo-TEM images of NMC particle after 50th discharge in 1.2 M LiPF$_6$–EC/DMC (A) and 1.2 M LiTFSI–AN–FM (B). (C) XPS chemical analysis of CEI layers for the pristine NMC (i) and cycled NMC in 1.2 M LiPF$_6$–EC/EMC (ii) and 1.2 M LiTFSI–AN–FM (iii).

increase of electrolyte side reactions and the instability of the SEI/CEI at elevated temperatures.

2.5. Interface characterizations

The chemistry and structure of cycled Li–NMC interfaces (CEI, SEI) were characterized by cryogenic-(scanning) transmission electron microscopy (cryo-(S)TEM) and X-ray photoelectron spectroscopy (XPS). Cryo-TEM was applied on cycled NMC622 to preserve the cathode electrolyte interphase (CEI) from beam damage.[33] After 50th discharge, the CEI in carbonate-based electrolytes shows significant variations in both thickness and distribution (Fig. 6A). This result is consistent with the observation in EDS under STEM mode (Fig. S24, ESI†), that the CEI of the same NMC particle displays a different phosphorus distribution at different planes. In contrast, the CEI generated in the liquefied gas electrolyte exhibits a much more uniform thickness with good surface coverage (Fig. 6B). This agrees with the relatively uniform sulfur distribution observed in STEM-EDS (Fig. S25, ESI†). XPS of cycled NMC also captures the S 2p signal in the liquefied gas electrolyte and shows different chemistry in various electrolytes (Fig. S26, ESI† and Fig. 6C). After being cycled in carbonate-based electrolyte, the oxygen ratio largely increased and the shape of carbon peak changed, indicating the formation of an organic-like CEI layer. Whereas the CEI formed using the liquefied gas electrolyte shows a

similar carbon peak found in the pristine NMC with less oxygen increase and absence of free AN also leads to improved CEI. Additionally, LiF, S–O, N–O species are formed by the decomposition of LiTFSI and FM, which are believed to promote a protective interphase.[43]

Depth-profiling XPS was also applied to cycled Li metal anode interfaces in different electrolytes (Fig. S27–S29, ESI†). Consistent with previously studies,[25,26] the liquefied gas electrolyte forms an inorganic-rich SEI by decomposition of FM, CO$_2$, and TFSI$^-$, enabling a robust interface for aggressive Li metal cycling. The detailed discussion and comparison to the carbonate electrolyte are included in the ESI.†

3. Conclusion

By introducing an AN cosolvent and increasing salt concentration, we developed a liquefied gas electrolyte with unique physical and chemical properties that supports rapid ion transport and desolvation, and shows impressive Li-metal compatibility, high anodic stability, and wide temperature operation window. The unique solvation structure uncovered by Raman and MD simulations show that all AN cosolvents are fully solvated to Li$^+$ and FM is partially coordinated with Li$^+$ with short residence times allowing fast exchange and desolvation. This ideal solvent-cosolvent combination yields superior

2216 | *Energy Environ. Sci.*, 2020, **13**, 2209–2219

This journal is © The Royal Society of Chemistry 2020

transport properties, including high low-temperature conductivity (4.8 mS cm^{-1} at −78 °C), expanded high-temperature operation range (from +40 °C to >+75 °C), and high transference number. Systems using the liquefied gas electrolyte formed stable interfaces at both the Li-metal and the cathode sides. It enabled high Li-metal CE of 99.4% at high current density of 3 mA cm^{-2} and 3 mA h cm^{-2}, as well as stable cycling of 4.5 V Li–metal batteries in the wide-temperature range between +55 and −60 °C. The developed liquefied gas electrolyte presents a promising pathway towards next-generation high-energy Li–metal batteries with wide-temperature operations.

4. Experimental section

4.1. Materials

The salts lithium bis(fluorosulfonyl)imide (LiFSI) (99.9%) and lithium bis(trifluoromethane)sulfonimide (LiTFSI) (99.9%) were obtained from BASF. Fluoromethane (99.99%) was purchased from commercial sources. 1.2 M LiPF$_6$ in EC/EMC 3:7 was purchased from BASF. Acetonitrile (AN, anhydrous, 99.8%), 1,2-dimethoxyethane (DME, 99.5%), and 1,3-dioxolane (DOL, 99.8%) were purchased from Sigma-Aldrich and stored over molecular sieves. The NMC622 (A-C023) was obtained from Argonne national laboratory.

4.2. Electrochemical measurements

Electrolytic conductivity measurements were performed in custom fabricated high-pressure stainless-steel coin cells, using polished stainless-steel (SS 316L) as both electrodes. The cell constant was calibrated from 0.447 to 80 mS cm^{-1} by using OAKTON standard conductivity solutions.

The Li$^+$ transference number is measured by the potentiostatic polarization method with an applied voltage of 10 mV. Electrochemical impedance spectroscopy was collected by a Biologic SAS (SP-200) system and the spectra were then fitted using ZView software.

Battery cycling test was performed by an Arbin battery test station (BT2043, Arbin Instruments, USA) in custom designed high-pressure stainless-steel coin cells, with Li metal (FMC lithium, 1 mm thickness, 1/4 inch diameter) as the counter electrode and a polished SS316L as the working electrode. A single 25 μm porous polypropylene separator (Celgard 2075) was applied for all the electrochemical experiments.

For Li metal plating and stripping experiments, lithium was first deposited onto the working electrode at 0.5 mA cm^{-2} until 0 V vs. Li and the voltage was held for 5 hours to form a stable SEI on the current collector. The first plating cycle was then started, followed by complete lithium stripping to a 1 V vs. Li cut off voltage. The CE was calculated as the Li stripping capacity divided by the Li plating capacity during a single cycle. For the test in different temperatures, the cells were soaked at the testing temperature in a temperature chamber (Espec) for several hours before cycling. In Li–NMC cycling, the cell was firstly cycled at C/10 rate at room temperature for 2 activation cycles and then cycled at selected rate and temperature.

4.3. Electrolyte addition

The liquefied gas electrolyte of 1.2 M LiTFSI, 1 M AN in FM:CO$_2$ 19:1 is labeled as 1.2 M LiTFSI–AN–FM. 1 M AN cosolvent is around 5% in volume. As similarly used in the previous study,[25] addition of 5 wt% CO$_2$ is added to helps stabilize the Li-metal anode. Electrolyte addition procedures have been described previously.[25]

4.4. Material characterization

Raman spectra of liquefied gas electrolytes were carried on Renishaw inVia confocal Raman microscope with an excitation wavelength of 532 nm. All spectra were calibrated with Si (520 nm) and analyzed by Wire 3.4 software developed by Renishaw Ltd.

Cryogenic focused ion beam (cryo-FIB) (FEI Scios DualBeam equipped with a CryoMat integrated cryo-stage and air-free quick loader) was applied to explore the morphology of the cross-section of electrochemically deposited Li. To minimize the beam damage during FIB operation, the samples are cooled down to −170 °C under continuous chilled nitrogen gas cooling at high vacuum (∼10^{-6} mbar). The cross-sections were firstly rough milled with a cross-sectional cut (30 kV, 5 nA) followed by a cross-sectional cleaning cut (30 kV, 0.5 nA).

X-Ray photoelectron spectroscopy (XPS) was performed using a Kratos AXIS Supra DLD XPS with monochromatized Al Kα radiation (λ = 0.83 nm and hν = 1486.7 eV) under a base pressure <10^{-8} Pa. To avoid moisture and air exposure, samples were transferred to the XPS chamber directly from a glovebox via vacuum transfer. All spectra were calibrated with hydrocarbon C 1s (284.6 eV) and analyzed by CasaXPS software. To remove residual salt on the surface, all samples were slightly rinsed with DMC and dried in glovebox antechamber before analysis.

Cryo-(S)TEM. After cycling, all cells were disassembled in an argon-filled glove box. The cathode was scraped off from current collector and dispersed in DMC solvent with the help of sonication. The obtained suspension containing dispersed particles were dropped on TEM lacey carbon grid which was then thoroughly dried under vacuum to remove residue DMC solvent. The loading and transferring the grid to TEM were carefully controlled to prevent sample from air exposure and detail information can be found in our previous publication.[33] HRTEM was recorded on a field emission gun JEOL-2800 at 200 kV with Gatan OneView Camera (full 4 K × 4 K resolution). STEM-EDS was performed on primary particles a at annular dark field (ADF) mode using the same microscope. All ADF images were acquired at 200 kV with a beam size of ≈5 Å. Note that both HRTEM and STEM-EDS were carried out under cryogenic temperature (∼180 °C) to minimize beam damage on CEI structure/chemistry.

4.5. Computational methods

MD simulation cell contained 2000 FM, 120 AN and 144 LiTFSI. A polarizable force field APPLE&P[44] with the previously developed LiTFSI, FM and AN parameters was used.[26,29] The length

of equilibration and production runs, simulation temperatures and predicted parameters are summarized in Table S1 (ESI†). The experimental density estimation was difficult at higher temperatures (+40 and +60 °C) due to the changes of liquid phase volume and composition ratios, therefore, compressed states with densities at lower temperatures were applied to interpret high-temperature cases (Table S1, ESI†). The equations of motions were solved with a time reversible (RESPA) integrator over the following time resolutions: (i) the contribution from bonds and angles to the forces were calculated at any 0.5 femtosecond (fs), (ii) the contribution of dihedrals and non-bonded forces within 8 Å cut-off were updated at any 1.5 fs, and iii) the remainder of the forces (reciprocal space Ewald and non-bonded forces within 14 or 16 Å cut-off were updated at any 3 fs. Nose–Hoover thermostat was used for temperature control. An archive containing all input files needed to perform bulk MD simulations is included in ESI.† The Li^+ cation transference number (t_+) was extracted from MD simulations following formalism suggested by Wohde et $al.$[45] using decomposition of the full charge displacement matrix into the contributions from cation–cation, cation–anion and anion–anion denoted as κ_{++}, κ_{+-} and κ_{--}. Note that κ_{+-} is defined using the opposite sign from Wohde et $al.$[45] The transference number (t_+) is defined using two parameters α, β (see Table S1, ESI†)

$$\alpha = \kappa_{++}/(\kappa_{++} + \kappa_{--}) \quad \text{and} \quad \beta = -2\kappa_{+-}/(\kappa_{++} + \kappa_{--}) \qquad (1)$$

$$\kappa = \kappa_{++} + \kappa_{++} + 2\kappa_{+-} \qquad (2)$$

$$t_+ = (\beta^2 - 4\alpha + 4\alpha^2)/(4(1 - \alpha)(\beta - 1)) \qquad (3)$$

Parameter α is similar to the transport number determined using self-diffusion coefficients. Parameter β is 0.92–0.98 indicates strong ion correlations to t_+.

Author contributions

Y. Yang, Y. Yin, C. S. R., and Y. S. M. conceived the idea and designed the experiments. Y. Yang, Y. Yin, D. M. D., Y. Z., M. M., and E. S. S. conducted the electrochemical experiments. O. B. developed force field and carried out the MD simulations with assist of D. M. D. Y. Yang performed the cryo-FIB, XPS characterization under J. Z. L.'s guidance. M. Z. carried out cryo-TEM. Y. Yin and E. S. S. performed Raman with S. W.'s interpretation based on D. M. D.'s cell design. Y. Yang prepared the manuscript with input from all co-authors. All authors have given approval to the final version of the manuscript.

Conflicts of interest

Patent applications relating to this work include PCT/US14/066015, PCT/US17/29821, and PCT/US2019/032414. Y. Shirley Meng is a member of the scientific advisory board for South 8 Technologies.

Acknowledgements

References

1 S. Chu and A. Majumdar, Opportunities and challenges for a sustainable energy future, $Nature$, 2012, **488**, 294–303.

2 J. W. Choi and D. Aurbach, Promise and reality of post-lithium-ion batteries with high energy densities, $Nat.$ $Rev.$ $Mater.$, 2016, 1–16, DOI: 10.1038/natrevmats.2016.13.

3 D. Lin, Y. Liu and Y. Cui, Reviving the lithium metal anode for high-energy batteries, $Nat.$ $Nanotechnol.$, 2017, **12**, 194–206.

4 P. Albertus, S. Babinec, S. Litzelman and A. Newman, Status and challenges in enabling the lithium metal electrode for high-energy and low-cost rechargeable batteries, $Nat.$ $Energy$, 2018, **3**, 16–21.

5 X. B. Cheng, R. Zhang, C. Z. Zhao and Q. Zhang, Toward Safe Lithium Metal Anode in Rechargeable Batteries: A Review, $Chem.$ $Rev.$, 2017, **117**, 10403–10473.

6 J. Liu, et $al.$, Pathways for practical high-energy long-cycling lithium metal batteries, $Nat.$ $Energy$, 2019, **4**, 180–186.

7 K. Xu, Nonaqueous liquid electrolytes for lithium-based rechargeable batteries, $Chem.$ $Rev.$, 2004, **104**, 4303–4417.

8 M. Li, C. Wang, Z. Chen, K. Xu and J. Lu, New Concepts in Electrolytes, $Chem.$ $Rev.$, 2020, DOI: 10.1021/acs.chemrev.9b00531.

9 K. Xu, Electrolytes and Interphases in Li-Ion Batteries and Beyond, $Chem.$ $Rev.$, 2014, **114**, 11503–11618.

10 C.-C. Su, et $al.$, Solvating power series of electrolyte solvents for lithium batteries, $Energy$ $Environ.$ $Sci.$, 2019, **12**, 1249–1254.

11 D. Aurbach, Review of selected electrode-solution interactions which determine the performance of Li and Li ion batteries, $J.$ $Power$ $Sources$, 2000, **89**, 206–218.

12 J. Qian, *et al.*, High rate and stable cycling of lithium metal anode, *Nat. Commun.*, 2015, **6**, 1–9.

13 S. Jiao, *et al.*, Stable cycling of high-voltage lithium metal batteries in ether electrolytes, *Nat. Energy*, 2018, **3**, 739–746.

14 S. J. Cho, *et al.*, Nonflammable Lithium Metal Full Cells with Ultra-high Energy Density Based on Coordinated Carbonate Electrolytes, *iScience*, 2020, **23**, 100844.

15 X. Ren, *et al.*, Localized High-Concentration Sulfone Electrolytes for High-Efficiency Lithium-Metal Batteries, *Chem*, 2018, **4**, 1877–1892.

16 S. Chen, *et al.*, High-Efficiency Lithium Metal Batteries with Fire-Retardant Electrolytes, *Joule*, 2018, **2**, 2–8.

17 X. Fan, *et al.*, Non-flammable electrolyte enables Li-metal batteries with aggressive cathode chemistries, *Nat. Nanotechnol.*, 2018, **13**, 715–722.

18 X. Fan, *et al.*, All-temperature batteries enabled by fluorinated electrolytes with non-polar solvents, *Nat. Energy*, 2019, **4**, 882–890.

19 Y. Yamada, *et al.*, Unusual stability of acetonitrile-based superconcentrated electrolytes for fast-charging lithium-ion batteries, *J. Am. Chem. Soc.*, 2014, **136**, 5039–5046.

20 Z. Hu, *et al.*, Nonflammable Nitrile Deep Eutectic Electrolyte Enables High-Voltage Lithium Metal Batteries, *ACS Appl. Mater. Interfaces*, 2020, **32**, 3405–3413.

21 Y. G. Cho, Y. S. Kim, D. G. Sung, M. S. Seo and H. K. Song, Nitrile-assistant eutectic electrolytes for cryogenic operation of lithium ion batteries at fast charges and discharges, *Energy Environ. Sci.*, 2014, **7**, 1737–1743.

22 X. Q. Zhang, *et al.*, Regulating Anions in the Solvation Sheath of Lithium Ions for Stable Lithium Metal Batteries, *ACS Energy Lett.*, 2019, **4**, 411–416.

23 Y. Zheng, *et al.*, Localized high concentration electrolyte behavior near a lithium-metal anode surface, *J. Mater. Chem. A*, 2019, **7**, 25047–25055.

24 Z. Wang, *et al.*, An Anion-Tuned Solid Electrolyte Interphase with Fast Ion Transfer Kinetics for Stable Lithium Anodes, *Adv. Energy Mater.*, 2020, **10**, 1–9.

25 C. S. Rustomji, *et al.*, Liquefied gas electrolytes for electrochemical energy storage devices, *Science*, 2017, **356**, 6345.

26 Y. Yang, *et al.*, High-Efficiency Lithium-Metal Anode Enabled by Liquefied Gas Electrolytes, *Joule*, 2019, **3**, 1986–2000.

27 X. Dong, Z. Guo, Z. Guo, Y. Wang and Y. Xia, Organic Batteries Operated at −70 °C, *Joule*, 2018, **2**, 902–913.

28 X. Dong, *et al.*, High-Energy Rechargeable Metallic Lithium Battery at −70 °C Enabled by a Cosolvent Electrolyte, *Angew. Chem.*, 2019, **131**, 5679–5683.

29 J. Chen, *et al.*, Improving Electrochemical Stability and Low-Temperature Performance with Water/Acetonitrile Hybrid Electrolytes, *Adv. Energy Mater.*, 2020, **10**, 1–10.

30 S. Chen, *et al.*, High-Efficiency Lithium Metal Batteries with Fire-Retardant Electrolytes, *Joule*, 2018, **2**, 1548–1558.

31 D. M. Seo, *et al.*, Solvate structures and spectroscopic characterization of LITFSI electrolytes, *J. Phys. Chem. B*, 2014, **118**, 13601–13608.

32 S. Zugmann, *et al.*, Electrochimica Acta Measurement of transference numbers for lithium ion electrolytes via four different methods, a comparative study, *Electrochim. Acta*, 2011, **56**, 3926–3933.

33 J. Alvarado, *et al.*, Bisalt ether electrolytes: A pathway towards lithium metal batteries with Ni-rich cathodes, *Energy Environ. Sci.*, 2019, **12**, 780–794.

34 O. Borodin, *et al.*, Modeling Insight into Battery Electrolyte Electrochemical Stability and Interfacial Structure, *Acc. Chem. Res.*, 2017, **50**, 2886–2894.

35 A. P. Abbott and C. A. Eardley, Conductivity of $(C_4H_9)_4N$ BF_4 in liquid and supercritical hydrofluorocarbons, *J. Phys. Chem. B*, 2000, **104**, 9351–9355.

36 J. Chen, *et al.*, Electrolyte design for Li metal-free Li batteries, *Mater. Today*, 2020, DOI: 10.1016/j.mattod.2020.04.004.

37 J. Z. Lee, *et al.*, Cryogenic Focused Ion Beam Characterization of Lithium Metal Anodes, *ACS Energy Lett.*, 2019, **4**, 489–493.

38 K. Yan, *et al.*, Temperature-dependent Nucleation and Growth of Dendrite-Free Lithium Metal Anodes, *Angew. Chem.*, 2019, **94025**, 11486–11490.

39 J. Wang, *et al.*, Improving cyclability of Li metal batteries at elevated temperatures and its origin revealed by cryo-electron microscopy, *Nat. Energy*, 2019, **4**, 664–670.

40 C. Fang, *et al.*, Quantifying inactive lithium in lithium metal batteries, *Nature*, 2019, **572**, 511–515.

41 W. A. Henderson, Concentrated electrolytes: decrypting electrolyte properties and reassessing Al corrosion mechanisms, *Energy Environ. Sci.*, 2014, **7**, 416–426.

42 M. B. Effat, *et al.*, Towards succinonitrile-based lithium metal batteries with long cycle life: The influence of fluoroethylene carbonate loading and the separator, *J. Power Sources*, 2019, **436**, 226802.

43 T. Li, X. Q. Zhang, P. Shi and Q. Zhang, Fluorinated Solid-Electrolyte Interphase in High-Voltage Lithium Metal Batteries, *Joule*, 2019, **3**, 2647–2661.

44 O. Borodin, Polarizable force field development and molecular dynamics simulations of ionic liquids, *J. Phys. Chem. B*, 2009, **113**, 11463–11478.

45 F. Wohde, M. Balabajew and B. Roling, Li$^+$ Transference Numbers in Liquid Electrolytes Obtained by Very-Low-Frequency Impedance Spectroscopy at Variable Electrode Distances, *J. Electrochem. Soc.*, 2016, **163**, A714–A721.

This journal is © The Royal Society of Chemistry 2020

Energy Environ. Sci., 2020, **13**, 2209–2219 | **2219**